Multi-color ultrafast laser platform for nonlinear optical imaging based on independently tunable optical parametric oscillators

**Shan Yang · Sanjay Adhikari · Manoj Dobbala · Sasidhar Adusumilli ·
Joseph D. Rowley · Feruz Ganikhanov · Lingquin Zhang · Glen Marrs ·
Robert Wysolmerski · George Spirou**

Abstract We report on design of a multi-color laser set up that allows for high spectral, time and spatial resolution imaging based on second- and third-order optical nonlinearities in soft condensed matter. Two femtosecond optical parametric oscillators (OPOs) are pumped simultaneously to provide intrinsically synchronized pulses at more than a dozen tunable colors across visible and infrared wavelengths. We demonstrate the use of independently tunable OPOs in a variety of imaging modalities. In one useful application, we explore brain tissue in a two-photon absorption fluorescence imaging experiment with near infrared optical pulses ($\lambda \sim 1{,}070$ nm). We also demonstrate second and sum-frequency generation microscopies in different tissues. Results from application of time-resolved, three-color coherent anti-stokes Raman scattering in tissue are presented to demonstrate feasibility of quantitative spectroscopic imaging.

1 Introduction

Bio-photonic and biomedical applications of fundamental nonlinear optical phenomena have become subjects of intensive efforts since they show a great potential in rapid and noninvasive characterization of cells and tissues on a molecular level. Multiphoton fluorescence microscopy [1], based on the nonlinear optical excitation of intrinsic or extrinsic fluorophores, is the most explored and developed technique. In many cases, the application of two-photon absorption fluorescence (TPAF) microscopy is implemented through molecular or, in some cases, quantum dot tagging of structures of interest, because the investigated specimen may lack natural fluorophores with high enough fluorescence yield. It is worth noting that, in the majority of implementations, TPAF experiments utilized a mode-locked Ti:sapphire laser source. Utilization of laser sources at wavelengths longer than the range covered by the Ti:sapphire laser would be very important from the standpoint of enhancing experimental capabilities. Second harmonic generation (SHG) [2], third harmonic generation (THG) [3, 4], coherent anti-stokes Raman scattering (CARS), and closely related stimulated Raman scattering (SRS) [5, 6] are key nonlinear optical techniques that provide label-free imaging of biological media with multimodal approach providing complementary information and additional benefits in biological media characterization [7].

Example applications for nonlinear microscopy include SHG microscopy experiments that showed tracking of time-resolved fluctuations of membrane potential [8] and imaging collagen-type-I structures [9], microtubules [10] and myosin of skeletal muscle [11, 12]. Likewise, CARS and THG microscopy has been successfully demonstrated to image cellular structures within mouse tissue [13], the collagen sheets of fascia [7], lipids [14, 15], and lipid storage [16] in living organisms.

Key technical point in each experimental implementation of nonlinear optical microscopy study is design and characteristics of ultrashort pulse laser source (e.g., peak power, wavelength of operation, repetition rate). In order to enable resonant nonlinear microscopy, such as CARS, SRS, TPAF or resonant sum-frequency generation (SFG)

S. Yang · S. Adhikari · M. Dobbala · S. Adusumilli ·
J. D. Rowley · F. Ganikhanov (✉)
Department of Physics, West Virginia University,
PO BOX 6315, Morgantown, WV 26506, USA
e-mail: feruz.ganikhanov@mail.wvu.edu

L. Zhang · G. Marrs · R. Wysolmerski · G. Spirou
Center for Neuroscience, West Virginia University,
1 Medical Center drive, Morgantown, WV 26506, USA

[17], tunable laser pulses are required. From a technical point of view, CARS or SRS are the most challenging methods and, therefore, most of the efforts applied so far have been focused on design and development of laser sources for coherent Raman-based microscopy.

In the very first attempt, the CARS microscopy technique was implemented in a degenerate two-color configuration whereby two independently tunable, synchronously pumped dye lasers provided intense ps duration laser pulses in the 565–620 nm and 620–700 nm spectral ranges [18]. Images of onion-skin-cells have been obtained with 0.7 μm spatial resolution using the CARS signal produced by the 2,450 cm^{-1} band of deuterated water. Interest in CARS microscopy was renewed a decade ago after Zumbush et al. [4] had reported CARS microscopy experiments in biological cells targeting Raman active vibrations using two independently tunable femtosecond pulses delivered by an optical parametric amplifier system running at a repetition rate of 1 kHz. Later, in a similar approach, to facilitate spectral selectivity and to obtain CARS spectra with fair resolution, Hashimoto et al. [19] employed a narrow bandwidth picosecond laser. CARS microscopy implementation using a high-repetition rate (~100 MHz) source was reported by Potma et al. [20]. In the cited work, two independently tunable picosecond Ti:sapphire lasers have been electronically synchronized to minimize jitter times to less than 20 fs and to provide two colors at wavelengths of 850 and 750 nm, respectively. This approach improved signal-to-noise ratio and provided images of 3T3 mouse fibroblast cells while targeting a vibration frequency of 1,570 cm^{-1}. Kee et al. [21] reported further progress in developing a Ti:sapphire-based CARS microscopy system with ultrashort pulses selected from a broadband continuum. The Ti:sapphire-based master oscillator source was used by Andresen et al. [22] and later by Ivanov et al. [23] and Pegoraro et al. [24] to demonstrate a photonic crystal fiber (PCF)-based light source for generating tunable excitation pulses that are applicable to CARS microspectroscopy. This setup allowed for probing Raman active lines with frequencies spanning up to 4,000 cm^{-1} while spectral resolution was about 25 cm^{-1}. Petrov et al. [25] reported a system for CARS microspectroscopy based on a Nd:vanadate ps laser that generates a ps pulse continuum in nonlinear fiber providing tunable output. This design allowed accessing Raman vibrations in the range of 700–1,700 cm^{-1}. The main disadvantages of fiber-based continuum sources are low peak intensities and low spectral brightness. Also, significant intensity fluctuations affect the signal-to-noise ratio. An approach that circumvents these drawbacks is based on a dual-wavelength picosecond optical parametric oscillator (OPO) source [26, 27]. The signal and idler beams from picosecond, synchronously pumped OPO provided two tunable colors necessary for CARS microscopy. The OPO is continuously tunable with the frequency difference between the two beams spanning from 100 to 3,700 cm^{-1}.

In this work, we report on design and performance aspects of a multi-color femtosecond pulse laser set up with a target goal of applying it to imaging and characterization of biological media with high spectral and time resolution. The laser set up concept is based on two low threshold OPOs that are synchronously pumped by a single mode-locked Ti:sapphire oscillator running at 76 MHz. The OPOs produce intrinsically synchronized broadly tunable femtosecond pulses in the near and mid-infrared with hundreds of milliwatts of average power. We demonstrate high resolution imaging of biological tissue using four different nonlinear optical imaging modalities, including a three-color time-resolved CARS technique. We demonstrate imaging of cerebral cortex in mouse brain, collagen-rich mouse tendon and mouse muscle probed by SHG, SFG, and time-domain CARS microscopy. Multiple other colors are also available from the OPOs at lower average power (1–40 mW) that can be used to explore resonant second- and third-order nonlinearities of biological molecules.

2 Experimental design

A detailed layout of the experimental set up is shown in Fig. 1. Output power (~3.2–3.6 W) of a mode-locked Ti:sapphire oscillator (Coherent Mira HP) is split into three parts. A small fraction of about 50–150 mW is outcoupled through a side port of a Glan–Taylor prism that is preceded by half-wave plate. The main part (~3.1–3.5 W) of the beam is split into two equal parts. These two beams are then used to synchronously pump two OPOs that utilize high parametric gain periodically poled lithium tantalate (PPSLT) crystals. Detailed OPO characteristics and performance were reported in our recent publications [28, 29]. The PPSLT gain medium is a better alternative compared to a commonly used periodically poled lithium niobate (PPLN) due to its higher threshold for photorefractive damage. A set of data showing key OPO output characteristics is presented in Fig. 2. Typical threshold for the OPO with a 5 % output coupler and a pair of intracavity dispersion compensating prisms was less than 200 mW so that the available pump power was multiple times above the threshold. At that pump power level, the available parametric gain is as broad as ~250 nm [29] so that variations in physical length of the cavity would result in continuous tuning of the signal beam wavelengths within a broad range (~200 nm) while the OPO maintains fairly high (>100 mW) average power. Cavity length tuning allowed covering wavelength range of 1,060–1,270 nm at
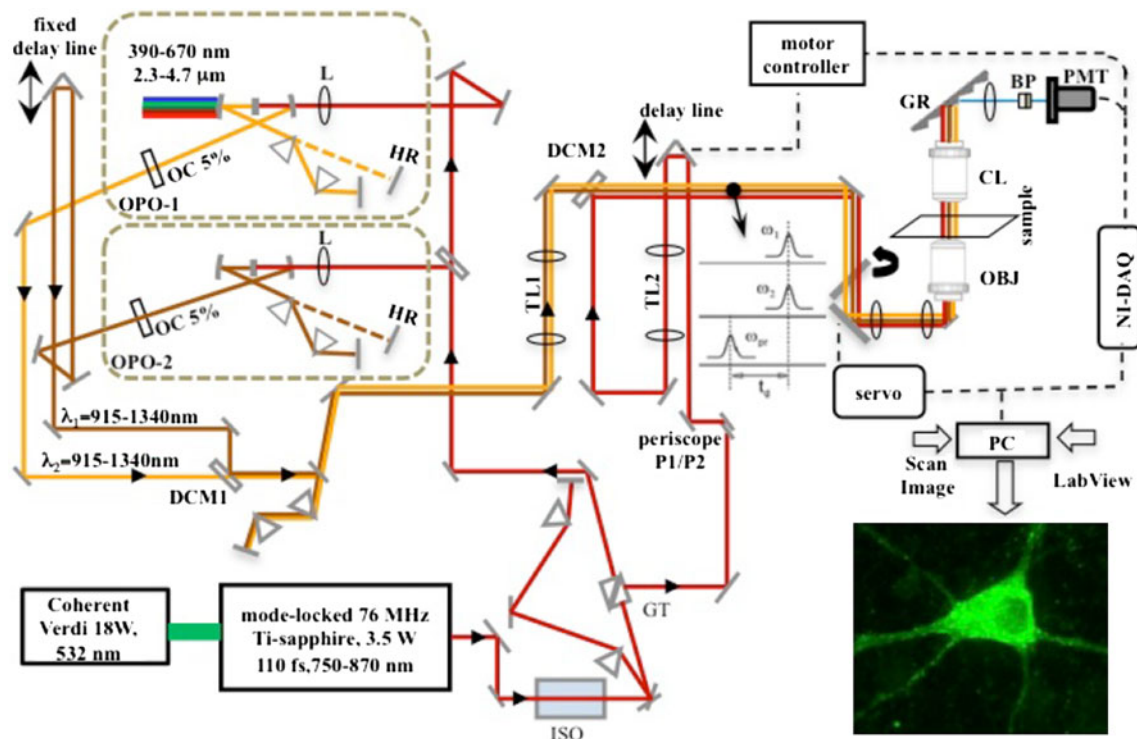
Fig. 1 Multi-color femtosecond laser platform for nonlinear optical imaging. Synchronized femtosecond pulses at three different colors were used to enable TPAF, SHF, SFG, and time-domain CARS microscopy. In time-domain CARS microscopy, two independently tunable pulses from OPOs (*yellow and brown lines*) served as excitation to phase-in molecular vibrations at ($\omega_1 - \omega_2$) while pulses from a small part of Ti:sapphire laser beam (*red lines*) were used as probe that tracked decay of the coherent polarization created by the OPO pulses. *ISO* optical isolator, *GT* Glan–Taylor prism, *OBJ* 60×, NA = 1.35 objective lens, *GR* 1,200 l/mm diffraction grating, *BP* bandpass filter, *DCM* dichroic mirror, *PMT* photomultiplier tube, *HR* highly reflecting mirror, *OC* output coupler, *TL* telescope

fixed quasi-phase-matching period ($\Lambda = 23$ μm), pump wavelength ($\lambda_p = 810$ nm) and temperature (T = 160 °C). Indeed, in the case of broadband gain, change in resonator's length would lead to central wavelength shift within the gain profile so that the net optical path length is unchanged thus matching pump pulse period that in turn results in maximum parametric gain. Pulse distortions [30, 31] have not been observed except for the edges of the tuning range and we again attribute this to the fact that the tuning was within the broadband range of parametric gain. In order to attain wavelengths beyond the mentioned range pump wavelength, QPM period and crystal temperature needed to be changed. Representative OPO spectra are shown in Fig. 2a. Stable transform limited pulse output with pulse widths in 110–160 fs range can be maintained throughout the entire tuning range provided that the intracavity prism insertion (prism spacing was set to 230 mm tip-to-tip) is adjusted to yield in net positive group dispersion delay (GDD). OPO operation at net zero GDD for the signal pulse would results in irregular shaped signal beam spectra and output with high intensity fluctuations similar to observations reported in earlier OPO studies [32]. However, at that GDD setting, pulses shorter than the pump pulse (<90 fs) can be generated. Typical signal and idler pulse autocorrelations at net positive GDD (i.e., regular shape and central wavelength stable spectra are maintained on long time scale) are shown in Fig. 2b, c, respectively. The idler beam wavelengths could be tuned to as far as 4.6 μm while average power of more than 50 mW is generated. The idler pulse spectrum at the far end of the OPO tuning range is shown in Fig. 2d. We have also performed dedicated cross-correlation measurements that would provide us with estimates of timing jitter between the two OPOs. By cross-correlating either signal pulses from the two OPOs or signal and pump pulses we were able to establish the upper level of timing jitter. The upper level value is estimated to be less than 8 fs. Furthermore, time-dependent four-wave mixing signal that involve the three pulses (see a typical data on Fig. 6c) indicates that we can measure transverse relaxation times (T_2) shorter than 130 fs. The crystal efficiency and amount of pump power permitted reaching a high pump depletion operating point (~ 70 %) so that, with intracavity loss of few percent, high average power (>400 mW) should be expected at the output according to steady state power solution for rate equations [33]. However, our major finding was that the power cannot be easily scaled and therefore reaching the above level in average power faced certain problems.
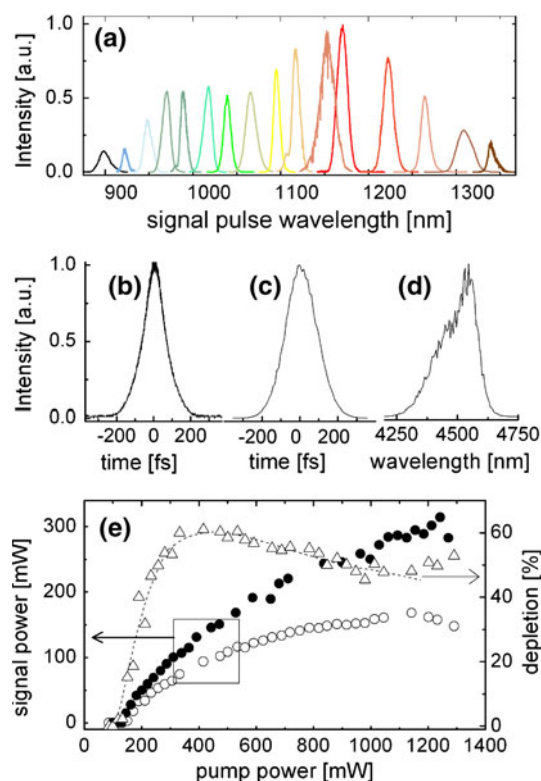
Fig. 2 OPO output pulse characteristics. Part (*a*) shows OPO pulse spectra obtained throughout available tuning range for the OPO. OPOs can be tuned within the 1,060–1,270 nm range by changing cavity length on micrometer scale while crystal temperature was fixed at 170 °C; the crystal poling period (Λ) was 23.0 μm and pump wavelength (λ_p) was set to 810 nm. For the 890–1040 nm range of tuning the above parameters were set to $\Lambda = 21.0$ μm, $\lambda_p = 740$ nm, and T = 150 °C. For the 1,240–1,350 nm range of tuning the parameters were set to $\Lambda = 24.2$ μm, $\lambda_p = 840$ nm, T = 160 °C. Spectral amplitudes indicate available OPO powers with respect to a maximum power of 320 mW achieved at 1,170 nm. Part (*b, c*) show typical pulse autocorrelations for signal ($\lambda_s = 1,070$ nm, $t_s = 111$ fs) and idler ($\lambda_i = 3.6$ μm, $t_i = 153$ fs) pulses (sec h^2 pulse shape is assumed). Part (*d*) shows idler pulse spectrum at ~4.5 μm while OPO can still deliver ~50 mW of average power in idler branch. Part (*e*) shows output power curves (*left scale*) for signal beam at short (less than 100 fs, *open circles*) and longer pulse (>160 fs, *filled circles*) mode operation. *Triangles* indicate the corresponding pump power depletion (*right scale*) at different pump power levels

The effect had been studied in details in our recent publication [29] and was attributed to intracavity power-dependent loss due to other nonlinear effects (e.g. self-focusing, etc.). As a result, power rollover occurs earlier if GDD is tuned to produce shorter pulses (i.e. higher peak powers). Part (e) of the figure shows a typical signal and idler beam power rollover at high pump power levels. A number of non-phase-matched processes in the crystals allowed generation of sum- and difference frequencies due to the interacting pump, signal and idler beams, thus providing from few to tens of milliwatts of power across the visible range. The signal beams of the two OPOs were combined and sent through a pair of dispersive prisms spaced 170 mm apart.

The prism sequence also provided dispersion pre-compensation to provide optimal pulse widths in the image plane. Telescopes were used to achieve optimal spot size matching between the three beams in the image plane. The three beams were directed to a galvo scanner (Cambridge Technology, Inc. model #6210) and imaged onto the entrance pupil of an objective lens. We have used high numerical aperture (NA ~ 0.9–1.35) and high magnification (40–60×) objective lenses. Due to various transmission losses within the optical train, about 30–35 % of the power generated by the OPOs could be delivered to the image plane, resulting in maximum power levels of about 60 mW for each beam. With the available full angle scan provided by galvo drivers, an area of about 200×200 μm^2 could be raster scanned at a maximum rate of 3 frames/second. In the detection arm we used a high numerical aperture (NA ~ 0.9) condenser followed by a diffraction grating and a set of bandpass filters. This permitted efficient detection of the signal of interest on the background of other signals generated within focal volume. A photomultiplier tube (PMT) with high gain and quantum efficiency (Hamamatsu model #H9305) was used to detect signal photons at selected wavelengths. The output from the PMT was digitized by a high-speed data acquisition card (National Instruments, model 6201 DAQ).Scan Image software (http://openwiki.janelia.org/wiki/display/ephus/ScanImage) was used to form and display images in 3D using collected data points from the PMT and the galvo scanner controllers.

3 Imaging and microspectroscopy results

We have tested performance of the multi-color set up in a series of imaging and time-domain microspectroscopy experiments. Figure 3a shows a TPAF image of axons and nerve terminals in an in vitro live mouse brain stem slice. Precise morphology, size and position of nerve terminals are monitored at several stages of synapse formation. To obtain the images using two-photon excitation, projection neurons and their axons were labeled with fluorescent Alexa488-dextran conjugate (Molecular Probes, Inc.). The image was obtained by tuning the Ti:sapphire oscillator wavelength to 920 nm, which corresponds to the two-photon peak absorption band of the fluorescent marker. In another example of TPAF imaging (Fig. 3b), cortical brain tissue from a 3-week-old mouse was investigated using femtosecond OPO radiation at 1,070 nm. The brain was perfusion-fixed and the cerebral cortex removed and held between two glass coverslips. Here, expression of a red fluorescent protein (tdTomato), controlled by the Six3 gene and Cre-mediated recombination, was restricted mostly to excitatory neurons in layer 4. The pial surface defined the

plane for image collection. Fluorescent neurons in layer 4 are about 300–500 μm deep to the pial surface. This initial experiment proves the feasibility of imaging neurons in deep cortical layers, which has been performed in living animals without compromising brain integrity. We have also tested sensitivity of the set up in second harmonic and sum-frequency generation (SHG and SFG) imaging with near-IR OPO beams. Figure 4a shows SHG imaging of mouse muscle tissue taken at OPO wavelength tuned to

1,065 nm. A characteristic periodic pattern along the diagonal line of the image, which is also the muscle axis, corresponds to detection of multiple muscle sarcomeres in which myosin band is strongly highlighted. This is because the molecular structure of muscle myosin lacks a center of symmetry which gives rise to a strong SHG signal, as has been demonstrated in Refs. [34, 35]. The high SHG signal lines correspond to the so-called H-zones within an A-band if one refers to sarcomere structure provided by standard,
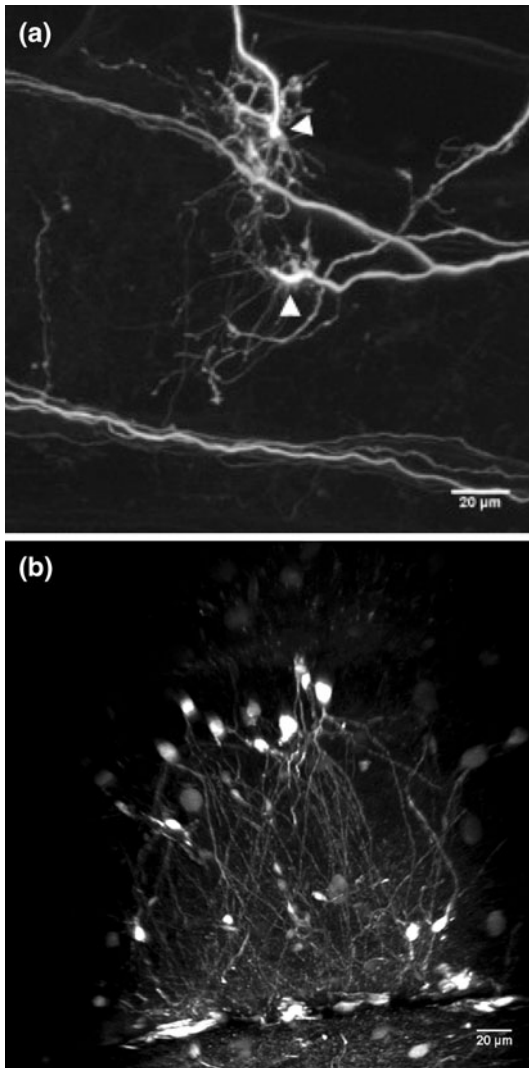

Fig. 3 a Two-photon absorption excited fluorescence image of mouse brainstem slice. The fluorescence was excited by femtosecond pulses from Ti:sapphire oscillator tuned to ~920 nm. Cochlear nucleus axons were selectively labeled by localized electroporation of fluorescent Alexa488-dextran conjugate. A high level of morphologic detail of the dynamic pre-synaptic structures (*arrowheads*) can be seen in the projection image stack. **b** TPAF image of cortical area of mouse brain tissue taken with the use of OPO tuned to 1,065 nm. Cortical brain tissue from a 3-week-old mouse, in which *red* fluorescent protein (tdTomato) expression, controlled by the Six3 gene, was restricted mostly to excitatory neurons in layer 4. Imaging of the intact cortex was done from the pial surface; fluorescent neurons in layer 4 are about 300–500 mm deep to the surface
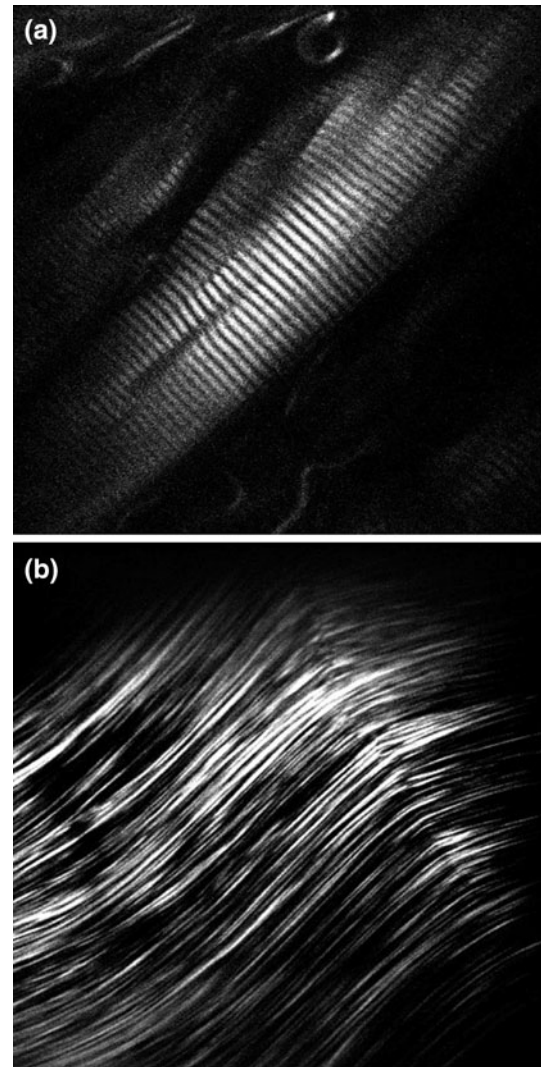

Fig. 4 a Second harmonic generation image (110×110 μm^2) of mouse skeletal muscle at fundamental wavelength of ~1,076 nm delivered by OPO. Muscle axis is along the image's diagonal and the periodic pattern shows several dozens of sarcomeric structures detected within the image area with skeletal muscle myosin bands contributing to strong SHG signal along lines perpendicular to the muscle axis. **b** Sum-frequency generation microscopy image of collagen bundle taken from mouse tail (image area-80×80 μm^2). Two OPO wavelengths were tuned to 965 and 1,170 nm, respectively, to generate SFG signal at ~520 nm

histology experiment-based description. Figure 4b shows image collagen bundles from tail of a rat taken in a sum-frequency generation (SFG) imaging experiment. In this case, the two OPOs were used with $\lambda_1 = 965$ nm, $\lambda_2 = 1{,}120$ nm, resulting in a SFG signal at around 520 nm. High contrast images can be obtained with only a few milliwatts of power delivered to the sample thereby minimizing photodamage (only after about 30 min) for combined OPO powers estimated at 90–120 mW in sample.

Our primary goals were to combine powers of different imaging modalities and to perform quantitative characterization of key biological cell and tissue constituents using their unique molecular signatures. To achieve these goals, we applied significant effort to enable and optimize time-domain three-color CARS microscopy with flexibility to produce also high contrast TPAF, SHG/SFG, and THG images. CARS microscopy with time resolution was tested in a variety of bulk media. Figure 5a shows the time-domain CARS transient in oil when wavelengths of a pair of broadband femtosecond pulses from the two OPOs were tuned to provide the frequency difference $(\omega_1 - \omega_2)$ corresponding to Raman active vibration at $\sim 1{,}300$ cm^{-1}. The Raman shift matches vibration frequencies at around C=C symmetric rock and in-phase methylene twist vibrations. The pair of pulses phase-in individual molecular vibrations in the probed volume creating a macroscopic excitation that can be quantitatively described in terms of coherent amplitude $Q(t)$ [36]. In the case when amplitude and phase-relaxation processes due to inter- and intra-molecular interactions proceed on a time scale significantly

longer than the excitation and probe pulse widths, the absolute value of $Q(t)$ can be measured because the time-domain anti-stokes signal $I_{as}(t_d)$ can be expressed as following:

$$I_{as}(t_d) = \zeta |Q(t_d)|^2 I_{pr} l^2 \tag{1}$$

where ζ is a factor that takes into account various parameters for the laser beams involved, l is interaction length, and I_{pr} is the probe pulse intensity. The physics of phase-relaxation processes for vibration modes defines the properties of $Q(t)$. In the case when $Q(t)$ is a real function, dispersion of the resonant third-order susceptibility $\left(\chi^{(3)}(\omega_{as}, \omega_1, -\omega_2, \omega_{pr})\right)$ can be deduced from the time-domain CARS signal using the following formula [37]:

$$\chi^{(3)}(\omega_{as}, \omega_1, -\omega_2, \omega_{pr}) = \kappa \int_0^\infty \left(\frac{I_{as}(t)}{I_{as}(0)}\right)^{1/2} e^{i(\omega_1 - \omega_2)t} dt \tag{2}$$

where κ is a factor that combines molecular density, molecular tensor parameter and probe field coupling parameters. Thus, by measuring the time-domain CARS signal, both imaginary and real parts of $\chi^{(3)}$ can be obtained in one measurement through Fourier transform of the experimental data. This method provides a key advantage, in comparison with Raman-based coherent and spontaneous spectroscopy methods, in applications that target precise spectral features in the vicinity of Raman active resonances. Figure 5b, c represent dispersion of real and

Fig. 5 a Time-domain CARS transient obtained from oil when Raman active vibrations around 1,280 cm^{-1} were targeted. Fourier transform of the experimental time-domain CARS signal [see formula (2)] yields in dispersion of imaginary b and real c parts of the resonant third-order nonlinearity. Solid line in panel a is the best fit to CARS transient. Solid line in panels b and c are real and imaginary parts of complex double-peak Lorentzian function

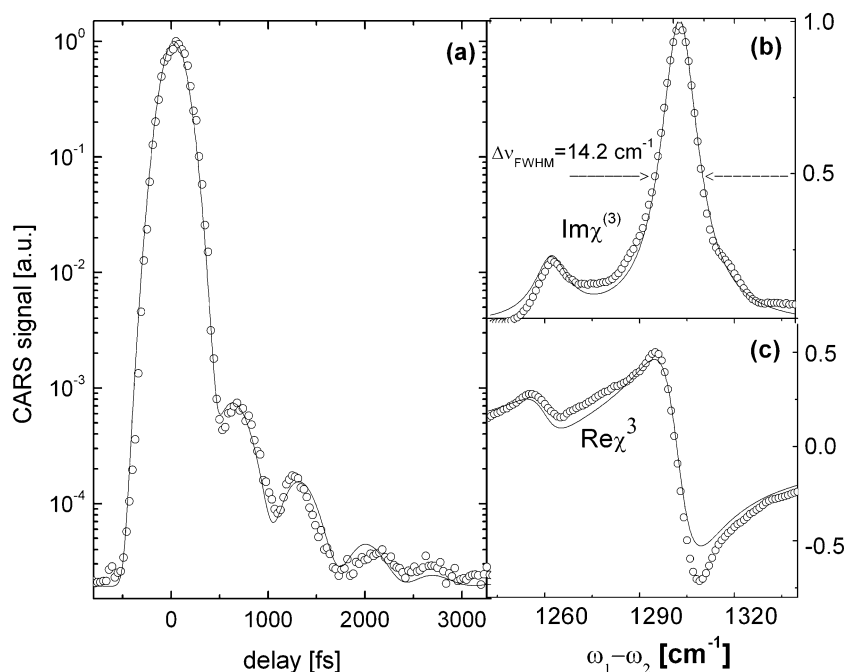**Fig. 6 a** Adult mouse tissue imaged with SFG microscopy at a depth of ~ 250 µm below epidermis layer. Collagen-rich part of adipose connective tissue generates a strong SFG signal in the upper right part of the image. **b** The same area imaged by CARS shows a dense fatty structure that is not detectable by SHG or SFG. Size of the images in panels **a** and **b** is 70×40 µm^2. To produce the CARS image OPOs were tuned to provide a frequency difference of $\sim 1,270$ cm^{-1}. **c** Time-domain CARS replica (*open circles*) obtained from smaller area within the fatty tissue in part **b** using the indicated OPO parameters. *Solid line* in panel **c** is the instrument response function corresponding to nonresonant CARS signal from glass substrate
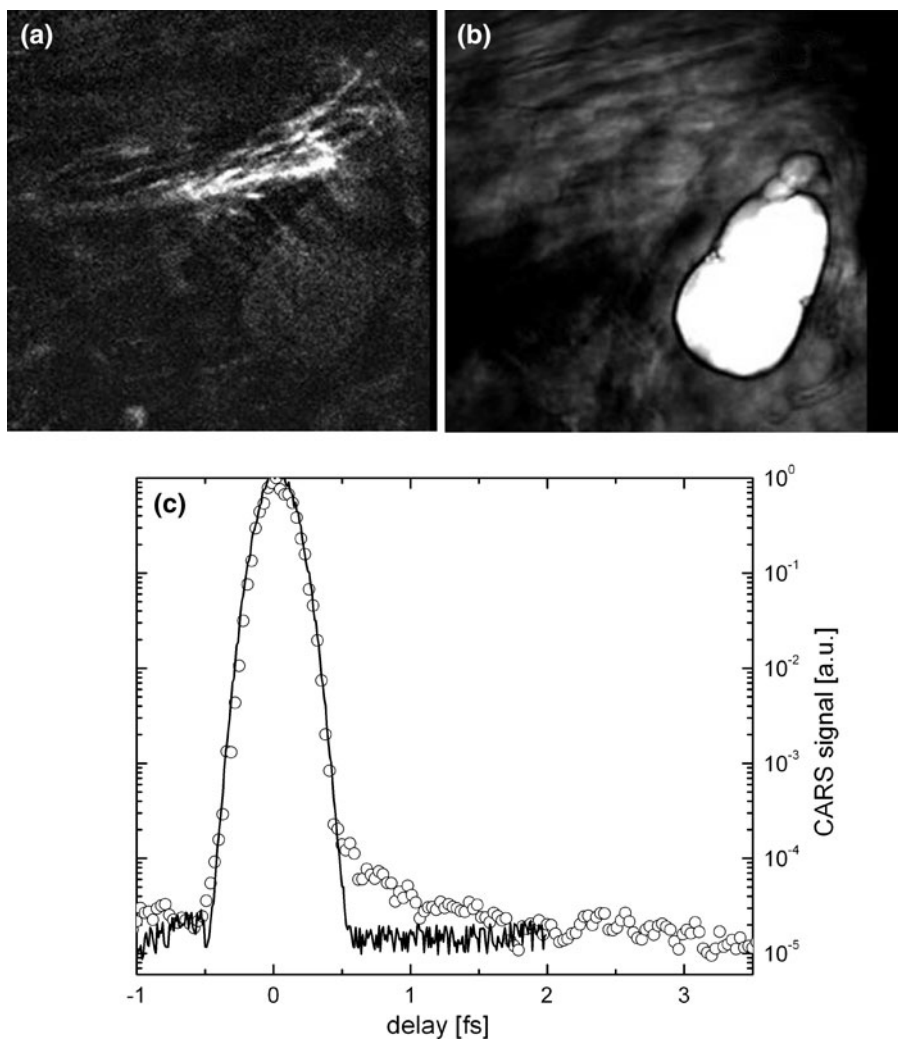
imaginary parts of $\chi^{(3)}$ in oil, respectively, that was obtained using experimentally measured time-domain CARS transient and formula (2). Two peaks can be precisely identified with each having 14.2 ± 0.2 cm^{-1} linewidth. With these data serving as a reference, we performed a time-domain measurement on mouse tissue with a specific focus on fat cells. Figure 6a shows an SFG image of the tissue where signal from a collagen-rich connective tissue within hypodermis layer is clearly seen. Figure 6b shows the same part of the tissue imaged with CARS when vibrations with Raman shift at $\omega_1 - \omega_2 \approx 1,280$ cm^{-1} were targeted. Comparison of the two images shows that the collagen-rich region is surrounded by fairly large fatty area that is faintly seen on the SFG image only when using high detector gains that also collect other background signals. Due to a relatively high molecular density of fat and due to its molecular composition, the CARS signal from that area overwhelms other resonant and nonresonant signals. We then tried to scan a narrower region within the fatty area while detecting the CARS

signal versus time delay of the probe pulse that was centered at 780 nm. The result of that experiment is shown in Fig. 6c. Though a much smaller signal is detected due to the resonant part, the experimental CARS transient captured dephasing of molecular vibrations which proceeds on the same time scale as phase decay for C=C rocking vibration in oil. Our conclusion is based on previous, extensive study of fats using spontaneous Raman spectroscopy [38, 39]. This quite promising result shows the feasibility of characterizing biological specimen with submicron spatial resolution using quantitative spectroscopy methods. The photodamage problem in experiments with high peak power pulses [40] is noticeable when the probe pulse average power is increased above 40 mW. We observed tissue dissection and decomposition within only a few minutes of imaging for femtosecond pulses at wavelengths up to 850 nm when a relatively large area (~ 50 µm^2) at scan rates of a few frames/s. Therefore, in future efforts we will explore configurations for longer wavelengths [26] to reduce the effects of photodamage.

In conclusion, we have demonstrated a versatile ultrafast laser set up that is based on high-repetition rate femtosecond optical parametric oscillators. The set up was designed for applications that target characterization of biological media using different nonlinear optical imaging modalities. The greatest advantage of the proposed approach is that using broadly tunable and well-synchronized near-IR pulses all major nonlinear optical imaging modalities are enabled across a much broader range of optical wavelengths. Most importantly, the approach opens another avenue in soft matter characterization. Namely, we have demonstrated that targeted microspectroscopy of key cell or tissue constituents can be performed within imaged specimen via their characteristic molecular signatures in Raman spectra.

References

1. W. Denk, J.H. Strickler, W.W. Webb, Two-photon laser scanning fluorescence microscopy. Science **248**(4951), 73–76 (1990)
2. P.J. Campagnola, A.C. Millard, M. Terasaki, P.E. Hoppe, C.J. Malone, W.A. Mohler, Three-dimensional high-resolution second-harmonic generation imaging of endogenous structural proteins in biological tissues. Biophys. J. **81**, 493–508 (2002)
3. D. Yelin, Y. Silberberg, Laser scanning third-harmonic generation microscopy in biology. Opt. Express **5**(8), 169 (1999)
4. D. Débarre, W. Supatto, E. Beaurepaire, Structure sensitivity in third-harmonic generation microscopy. Opt. Lett. **30**(16), 2134–2136 (2005)
5. A. Zumbusch, G.R. Holtom, X.S. Xie, Three-dimensional vibrational imaging by coherent anti-stokes Raman scattering. Phys. Rev. Lett. **82**(20), 4142–4145 (1999)
6. F.W. Christian, W. Min, B.G. Saar, S. Lu, G.R. Holtom, C. He, J.C. Tsai, J.X. Kang, X.S. Xie, Label-free biomedical imaging with high sensitivity by stimulated Raman scattering microscopy. Science **322**, 1857–1861 (2008)
7. C.P. Pfeffer, B.R. Olsen, F. Ganikhanov, F. Légaré, Multimodal nonlinear optical imaging of collagen arrays. J. Struct. Biol. **164**(1), 140–145 (2008)
8. R. Araya, J. Jiang, K.B. Eisenthal, R. Yuste, The spine neck filters membrane potentials. PNAS **103**(47), 17961–17966 (2006)
9. R.M. Williams, W.R. Zipfel, W.W. Webb, Interpreting second-harmonic generation images of collagen I fibrils. Biophys. J. **88**, 1377–1386 (2005)
10. D.A. Dombeck, K.A. Kasischke, H.D. Vishwasrao, M. Ingelsson, B.T. Hyman, W.W. Webb, Uniform polarity microtubule assemblies imaged in native brain tissue by second-harmonic generation microscopy. PNAS **100**(12), 7081–7086 (2003)
11. S.V. Plotnikov, A.C. Millard, P.J. Campagnola, W.A. Mohler, Characterization of the myosin-based source for second-harmonic

generation from muscle sarcomeres. Biophys. J. **90**(2), 693–703 (2006)
12. C.P. Pfeffer, B.R. Olsen, F. Ganikhanov, F. Légaré, Imaging skeletal muscle using second harmonic generation and coherent anti-stokes Raman scattering microscopy. Biomed. Opt. Express **2**(5), 1366–1376 (2011)
13. C.L. Evans, E.O. Potma, M. Puoris'haag, D. Cote, C.P. Lin, X.S. Xie, Chemical imaging of tissue in vivo with video-rate coherent anti-stokes Raman scattering microscopy. PNAS **102**(46), 16807–16812 (2005)
14. X. Nan, E.O. Potma, X.S. Xie, Nonperturbative chemical imaging of organelle transport in living cells with coherent anti-stokes Raman scattering microscopy. Biophys. J. **91**, 728–735 (2006)
15. D. Débarre, W. Supatto, A.-M. Pena, A. Fabre, T. Tordjmann, L. Combettes, M.-C. Schanne-Klein, E. Beaurepaire, Imaging lipid bodies in cells and tissues using third-harmonic generation microscopy. Nat. Methods **3**(1), 47–53 (2006)
16. T. Hellerer, C. Axäng, C. Brackmann, P. Hillertz, M. Pilon, A. Enejder, Monitoring of lipid storage in *Caenorhabditis elegans* using coherent anti-stokes Raman scattering (CARS) microscopy. PNAS **104**(37), 14658–14663 (2007)
17. V. Raghunathan, Y. Han, O. Korth, N. Ge, E.O. Potma, Rapid vibrational imaging with sum frequency generation microscopy. Opt. Lett. **36**(19), 3891–3893 (2011)
18. M.D. Duncan, J. Reintjes, T.J. Manuccia, Scanning coherent anti-stokes Raman microscope. Opt. Lett. **7**(8), 350–352 (1982)
19. M. Hashimoto, T. Araki, S. Kawata, Molecular vibration imaging in the fingerprint region by use of coherent anti-stokes Raman scattering microscopy with a collinear configuration. Opt. Lett. **25**(24), 1768–1770 (2000)
20. E.O. Potma, D.J. Jones, J.-X. Cheng, X.S. Xie, J. Ye, High-sensitivity coherent anti-stokes Raman scattering microscopy with two tightly synchronized picosecond lasers. Opt. Lett. **27**(13), 1168–1170 (2002)
21. T.W. Kee, M.T. Cicerone, Simple approach to one-laser, broad-band coherent anti-stokes Raman scattering microscopy. Opt. Lett. **29**(23), 2701–2703 (2004)
22. E.R. Andresen, C.K. Nielsen, J. Thøgersen, S.R. Keiding, Fiber laser-based light source for coherent anti-stokes Raman scattering microspectroscopy. Opt. Express **15**, 4848–4856 (2007)
23. A.A. Ivanov, A.A. Podshivalov, A.M. Zheltikov, Frequency-shifted megawatt soliton output of a hollow photonic-crystal fiber for time-resolved coherent anti-stokes Raman scattering microspectroscopy. Opt. Lett. **31**, 3318 (2006)
24. A.F. Pegoraro, A. Ridsdale, D.J. Moffatt, Y. Jia, J.P. Pezacki, A. Stolow, Optimally chirped multimodal CARS microscopy based on a single Ti:sapphire oscillator. Opt. Express **17**, 2984 (2009)
25. G.I. Petrov, V.V. Yakovlev, Enhancing red-shifted white-light continuum generation in optical fibers for applications in nonlinear Raman microscopy. Opt. Express **13**, 1299 (2005)
26. F. Ganikhanov, S. Carrasco, X.S. Xie, M. Katz, W. Seitz, D. Kopf, Broadly tunable dual-wavelength light source for coherent anti-Stokes Raman scattering microscopy. Opt. Lett. **31**, 1292 (2006)
27. M. Jurna, J.P. Korterik, H.L. Offerhaus, C. Otto, Noncritical phase-matched lithium triborate optical parametric oscillator for high resolution coherent anti-stokes Raman scattering spectroscopy and microscopy. Appl. Phys. Lett. **89**, 251116 (2006)
28. K.V. Bhupathiraju, A.D. Seymour, F. Ganikhanov, Femtosecond optical parametric oscillator based on periodically poled stoichiometric LiTaO$_3$ crystal. Opt. Lett. **34**, 2093 (2009)
29. J. Rowley, S. Yang, F. Ganikhanov, Power and tuning characteristics of a broadly tunable femtosecond optical parametric oscillator based on periodically poled stoichiometric lithium tantalate. J. Opt. Soc. Am. B **28**, 1036 (2011)

30. W.S. Pelouch, P.E. Powers, C.L. Tang, Ti:sapphire-pumped, high-repetition-rate femtosecond optical parametric oscillator. Opt. Lett. **17**, 1070–1072 (1992)

31. S. Akhmanov, A. Chirkin, K. Drabovich, A. Kovrigin, R. Khokhlov, A. Sukhorukov, Nonstationary nonlinear optical effects and ultrashort light pulse formation. IEEE J. Quantum Electron **4**, 598–605 (1968)

32. E.C. Cheung, J.M. Liu, Theory of a synchronously pumped optical parametric oscillator in steady-state operation. J. Opt. Soc. Am. B **7**, 1385–1401 (1990)

33. J.C. Bjorkholm, Some effects of spatially nonuniform pumping in pulsed optical parametric oscillators. IEEE J. Quant. Electron. **QE-7**, 109 (1971)

34. S.V. Plotnikov, A.C. Millard, P.J. Campagnola, W.A. Mohler, Characterization of the myosin-based source for second-harmonic generation from muscle sarcomeres. Biophys. J. **90**, 693 (2006)

35. C.P. Pfeffer, B.R. Olsen, F. Ganikhanov, F. Legare, Imaging skeletal muscle using second harmonic generation and coherent anti-stokes Raman scattering microscopy. Biomed. Opt. Express **2**, 1366 (2011)

36. A. Laubereau, W. Kaiser, Vibrational dynamics of liquids and solids investigated by picosecond light pulses. Rev. Mod. Phys. **50**, 607 (1978)

37. S. Yang, F. Ganikhanov. Dispersion of nonlinear optical susceptibility obtained with femtosecond time-domain coherent anti-stokes Raman scattering. Phys. Rev. Lett. (in review)

38. L.B. Lyndgaard, K.M. Sørensen, F. van den Berga, S.B. Engelsena, Depth profiling of porcine adipose tissue by Raman spectroscopy. J. Raman Spectrosc. **43**, 482 (2012)

39. O. Abbas, J.A. Fernández Pierna, R. Codony, C. von Holst, V. Baeten, Assessment of the discrimination of animal fat by FT-Raman spectroscopy. J. Mol. Struct. **924–926**, 294 (2009)

40. A. Hopt, E. Neher, Highly nonlinear photodamage in two-photon fluorescence microscopy. Biophys. J. **80**, 2029 (2001)